

The Indentation Size Effect: A Critical Examination of Experimental Observations and Mechanistic Interpretations

George M. Pharr,^{1,2,*} Erik G. Herbert,¹
and Yanfei Gao^{1,3}

¹Department of Materials Science & Engineering, University of Tennessee, Knoxville, Tennessee 37996-2200; email: pharr@utk.edu, eherbert@utk.edu, ygao7@utk.edu

²Materials Science & Technology Division and ³Computer Science & Mathematics Division, Oak Ridge National Laboratory, Oak Ridge, Tennessee 37831

Annu. Rev. Mater. Res. 2010. 40:271–92

First published online as a Review in Advance on
January 13, 2010

The *Annual Review of Materials Research* is online at
matsci.annualreviews.org

This article's doi:
10.1146/annurev-matsci-070909-104456

Copyright © 2010 by Annual Reviews.
All rights reserved

1531-7331/10/0804-0271\$20.00

*Corresponding author

Key Words

hardness, metals, strength, dislocations, nanoindentation, modeling

Abstract

The indentation size effect is one of several size effects on strength for which “smaller is stronger.” Through use of geometrically self-similar indenters such as cones and pyramids, the size effect is manifested as an increase in hardness with decreasing depth of penetration and becomes important at depths of less than approximately 1 μm . For spherical indenters, the diameter of the sphere is the most important length scale; spheres with diameters of less than approximately 100 μm produce measurably higher hardnesses. We critically review experimental observations of the size effect, focusing on the behavior of crystalline metals, and examine prevailing ideas on the mechanisms responsible for the effect in light of recent experimental observations and computer simulations.

ISE: indentation size effect

INTRODUCTION

Over the past several decades, interest in micro- and nanoscale deformation phenomena has grown enormously, driven largely by new technologies that require an understanding of how materials perform at small scales and by new imaging and characterization techniques that allow physical phenomena to be examined at ever-decreasing length scales. In the area of the mechanical behavior of materials, one of the more interesting small-scale phenomena is an increase in yield or flow strength that is often observed when the size of the test specimen is reduced to micrometer and submicrometer dimensions. Such size-dependent increases in strength are due to unique deformation phenomena that can be observed only when the specimen dimensions approach the average dislocation spacing and when plastic deformation is controlled by a limited number of defects.

For similar reasons, scale-dependent behavior is also observed in indentation testing when the size of the hardness impression is small, resulting in an indentation size effect (ISE). The ISE is most often observed for materials that are indented with geometrically self-similar indenters like pyramids and cones (see **Figure 1**). Assuming that plasticity can be described by classical continuum concepts, in which there is no inherent material length scale, and noting that there is no length scale for geometrically self-similar indenters, the hardness, H , defined as the load on the indenter normalized with respect to the projected contact area of the hardness impression (see **Figure 1**), should be independent of the depth of penetration, h . However, over the past 60 years,

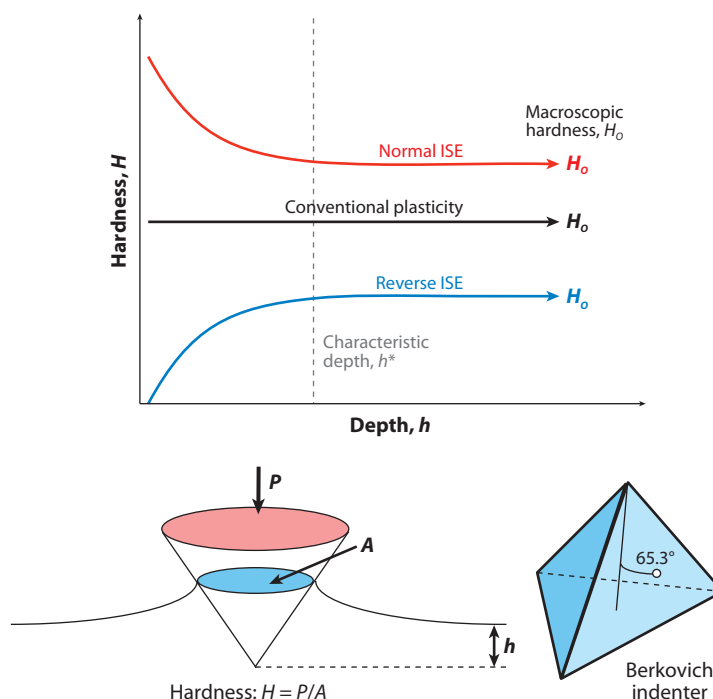


Figure 1

Schematic representation of the indentation size effect (ISE) for geometrically self-similar indenters such as a cone or pyramid. Normally, hardness, H , increases at small depths (the normal ISE), but some observations of decreasing hardness have also been reported (the reverse ISE). According to continuum plasticity, the hardness should be independent of depth. The hardness is defined as the ratio of the load on the indenter, P , to the projected area of contact of the hardness impression, A .

there have been numerous reports of significant variations of hardness with depth, especially at depths of less than a few micrometers (1–10). Two types of effects have been reported. In the more frequently seen effect—the normal ISE—the hardness increases at small depths, giving rise to the expression “smaller is stronger” (see **Figure 1**). However, in some cases, the hardness has been observed to decrease—the reverse ISE (2, 3, 5, 6, 11).

This review addresses the origin of these effects and the degree to which we understand them. The focus is on crystalline materials like metals and soft alkali halide salts in which plasticity is facilitated by dislocation glide processes and strength is determined by dislocation-dislocation interactions. Although ISEs have been reported for other classes of materials, e.g., ceramics, semiconductor materials, and amorphous materials, the mechanisms responsible for them may be very different, involving cracking, phase transformations, and non-dislocation-based mechanisms of plasticity (12–14). We focus also on the normal ISE, which is more frequently observed and thought to have its origins in fundamental material processes. The reverse ISE, in contrast, is usually ascribed to testing artifacts such as vibration in the testing system and/or problems with accurately imaging and measuring the sizes of hardness impressions at dimensions approaching the limits of optical microscopy (4–6).

EXPERIMENTAL OBSERVATIONS

Microhardness Testing

Historically, the ISE was first studied using Vickers microhardness testing, in which hardness is determined by imaging the residual plastic contact impressions made with a square-based diamond pyramid—a geometrically self-similar indenter with a centerline-to-face angle of 68° —and by measuring the contact area from an optically magnified image (1, 2, 5, 6). Early explanations for the ISE attributed it either to sample preparation problems, in particular, hardened surface layers due to polishing and/or hard surface oxides, or to indenter tip blunting, which causes a transition from self-similar geometry to spherical geometry at small contact depths. Nevertheless, careful studies in noble metals with carefully prepared surfaces led some investigators to suggest that the ISE is more fundamental than these explanations and is possibly caused by the limited numbers of dislocations that exist in small deformed volumes (3, 6).

Load- and Depth-Sensing Indentation

Although most of the early research on the ISE took place in the period roughly between 1950 and 1970, there was a significant rebirth of activity in the 1990s due to the advent of load- and depth-sensing testing, or nanoindentation (15–21). These techniques, which have the ability to determine the size of the hardness impression from indenter force-displacement curves rather than from microscopic measurement of the residual hardness impression, enabled researchers to explore and characterize the ISE to unprecedented small depths, as small as a few nanometers in some cases (15). The classic example of ISE data obtained in this way is that of McElhaney et al. (22). Shown in **Figure 2**, this frequently cited data set was generated by conducting experiments on a carefully prepared (111) Cu single crystal with a Berkovich indenter, a three-sided pyramid with a centerline-to-face angle of 65.3° (see **Figure 1**). This indenter, which has the same area-to-depth relationship as the four-sided Vickers pyramid, is preferred in nanoindentation testing because it can be prepared without the chisel edge tip defect that destroys the geometric self-similarity of the Vickers indenter at small depths. The data shown in **Figure 2** exhibit classic ISE behavior, specifically, a significant increase in hardness at depths below a few micrometers. Similar

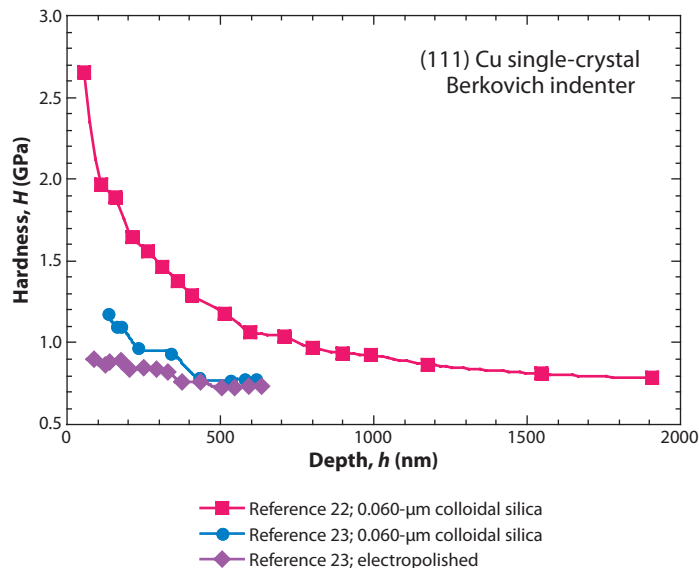


Figure 2

Indentation size effect (ISE) data for (111) Cu single crystals obtained in nanoindentation experiments. The classic data of McElhaney et al. (22) are frequently used in modeling efforts, but the data of Liu & Ngan (23) suggest that the magnitude of the ISE is very sensitive to surface preparation. All experiments shown here were performed with a Berkovich indenter.

increases have been observed in numerous other studies, with the characteristic length at which the hardness starts to increase typically being of the order of 1 μm .

Difficulties in Making Measurements

Although the Cu data of McElhaney et al. (22) show a very marked ISE, i.e., a hardness increase of more than a factor of two from large ($\sim 1 \mu\text{m}$) to small ($\sim 0.1 \mu\text{m}$) depths, making meaningful measurements of hardness at submicrometer depths is not a trivial task and one that is fraught with potential for error and misleading results. The reasons for this are numerous, ranging from difficulties in preparing surfaces free from mechanical damage (9, 23–25) to artifacts in nanoindentation testing and data analysis procedures (26, 27). To illustrate the importance of these potential errors, **Figure 2** includes two other data sets for (111) Cu, as measured in experiments by Liu & Ngan (23), that were designed to directly address the importance of surface preparation procedures. In one set of measurements, the ISE was measured for a crystal prepared nominally the same way as in McElhaney et al. (22), specifically, standard grinding followed by 20 min of polishing with 0.06- μm colloidal silica. Procedures like this are frequently used and are often recommended to prepare high-quality, relatively damage-free surfaces (28). However, it is clear from **Figure 2** that the data in the two studies are very different: The ISE as measured by Liu & Ngan (23) is significantly smaller. Although the exact reason for the difference is not clear, it may be due to the starting dislocation structure in the crystal (i.e., how the crystal was prepared and annealed) and/or to subtle differences in the grinding process, e.g., inadequate removal of damage from early parts of the grinding. In another set of experiments, also shown in **Figure 2**, Liu & Ngan (23) found that preparing the surface by electropolishing reduced the magnitude of the effect even more. Whatever the origin of these differences, surface preparation is extremely important, and from

this perspective, data reporting the ISE must be carefully scrutinized. We discuss below the issues of surface preparation in greater detail, but suffice it to say here that there are lingering questions about the adequacy of many of the experimental data sets used to characterize and quantify the ISE.

GND: geometrically necessary dislocation

MODELS AND MECHANISMS

Experimental observations like those in **Figure 2** led to a flurry of research activity, both experimental and theoretical, to further characterize and explain the ISE. Modeling efforts can be divided roughly into two types, depending on whether the model is mechanistically based (29–34), relying on dislocation descriptions of the hardening mechanisms, or phenomenological, introducing material length-scale parameters into conventional descriptions of continuum plasticity (35–39). Because the latter often invokes the concept of a plastic strain gradient, such approaches are commonly referred to as strain gradient plasticity models. They apply not only to indentation testing but also to any testing geometry, e.g., bending of small beams or torsion of fine wires, in which a plastic strain gradient is produced. Several strain gradient theories have been developed (35–39), and they are often tested or calibrated by comparison to ISE data. A detailed description of strain gradient theories is beyond the scope of this review, and we focus here on the mechanistically based models.

The Nix-Gao Model

Although numerous mechanistic models for the ISE have been proposed, the most widely used model to explain experimental observations is that developed by Nix & Gao (29). Shown schematically in **Figure 3a**, the model is based on the concept of geometrically necessary dislocations (GNDs), that is, dislocations that must be present near the indentation to accommodate the

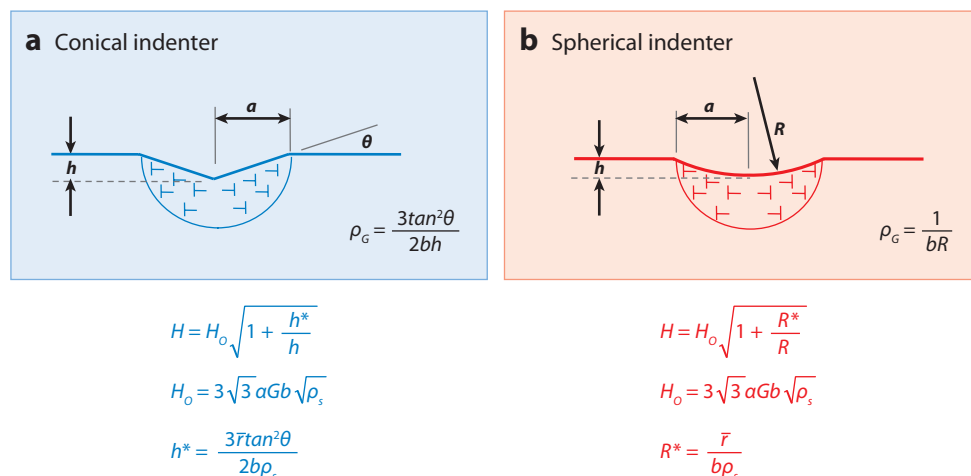


Figure 3

Schematic representation of the Nix-Gao (29) model for (a) conical indenters and (b) its extension to spherical indenters (41). In both scenarios, the geometrically necessary dislocations (GNDs) are assumed to reside in a hemispherical region beneath the indenter, whose radius is equal to the radius of contact, a , of the hardness impression. For conical indenters, the GND density is then inversely proportional to the depth of penetration, h , and for spheres, it is independent of depth but inversely proportional to the indenter radius, R .

volume of material displaced by the indenter at the surface. In the Nix-Gao model, the indenter is assumed to be a rigid cone whose self-similar geometry is defined by the angle, θ , between the indenter and the undeformed surface (see **Figure 3a**). The basic principle underlying the model is that the GNDs exist in addition to the usual statistically stored dislocations (SSDs) produced during uniform straining, giving rise to an extra hardening component that becomes larger as the contact impression decreases in size. Mathematically, this is implemented by assuming that the flow stress, σ , is related to the total dislocation density, ρ_T , through the Taylor relation,

$$\sigma = \sqrt{3}\alpha Gb\sqrt{\rho_T}, \quad 1.$$

where α is the Taylor factor, G is the shear modulus, and b is the Burger's vector. This is then combined with the Tabor relation,

$$H = 3\sigma, \quad 2.$$

to relate the hardness, H , to the flow stress, σ . In addition, two key assumptions are made: (a) that the total dislocation density is the simple mathematical sum of the geometrically necessary part, ρ_G , and the statistically stored part, ρ_S , that is, $\rho_T = \rho_G + \rho_S$ and (b) that the GNDs are constrained to reside within a hemispherical volume (see **Figure 3a**), where the radius of the volume is equal to the radius of contact of the indenter in the surface, a . Simple geometric considerations then lead to

$$\rho_G = (3 \tan^2 \theta)/(2bh). \quad 3.$$

This is a very important relation, as it contains the essential physics of the ISE; namely, the hardness increases at small depths because the geometrically necessary component of the dislocation density is inversely proportional to the depth and rises dramatically and without bound when the contact is small. Combining the above relations leads to

$$H = H_o \sqrt{1 + b^*/b}, \quad 4.$$

where $H_o = 3\sqrt{3}\alpha Gb\sqrt{\rho_s}$ represents the macroscopic hardness, i.e., the hardness that is asymptotically approached at large depths, and $b = (3 \tan^2 \theta)/(2b\rho_s)$ is the characteristic depth below which the extra hardening becomes appreciable. The characteristic depth depends on both material parameters (b and ρ_s) and geometric parameters (θ) and is thus not strictly a material constant. Other investigators (30) have modified the derivation to include the Nye factor, \bar{r} , which was first introduced by Arsenlis & Parks (40) to account for crystallographic constraints on the GND and SSD densities. It is defined such that $\rho_T = \bar{r}\rho_G + \rho_S$ and has a value of approximately 1.9 for FCC metals (40). With the Nye factor included, the characteristic depth becomes $b^* = (3\bar{r} \tan^2 \theta)/(2b\rho_s)$.

The primary test of the Nix-Gao model has been to compare its predictions to experimental data noting that

$$H^2 = H_o^2(1 + b^*/b), \quad 5.$$

implying that a plot of H^2 versus $1/b$ should be linear with an intercept of H_o^2 and a slope related to b^* . **Figure 4** shows such a plot for the Cu data of McElhaney et al. (22) and the Ag data of Ma & Clarke (20), both obtained with a Berkovich indenter. The remarkable linearity of these data sets at all but the smallest depths (large $1/b$) has served as the primary evidence for the Nix-Gao model. In both cases, the characteristic depth is of the order of 1 μm , implying that the ISE becomes significant at depths of approximately 1 μm and less.

The Indentation Size Effect for Spherical Indenters

Although the ISE as described thus far is one that applies strictly to geometrically self-similar indenters like pyramids and cones, there is an equally important ISE for spherical indenters.

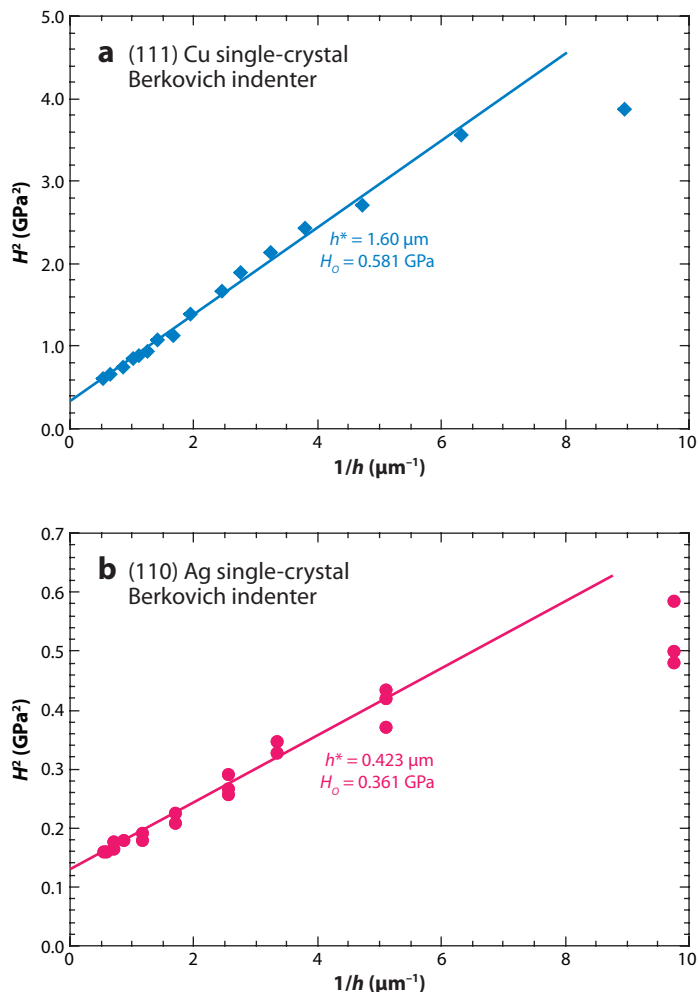


Figure 4

A plot of H^2 versus $1/h$ for (a) the (111) Cu data of McElhane et al. (22) and (b) the (110) Ag data of Ma & Clarke (20), both obtained in nanoindentation experiments with a Berkovich indenter. The extreme linearity of the data has been taken as the primary evidence for the Nix-Gao mechanism, although there are indications in both data sets that the linearity does not extend to very small depths (large $1/h$).

However, for spheres, the ISE is manifested not through the depth of penetration but rather through the radius of the sphere. This was demonstrated by Swadener et al. (41), who conducted indentation experiments on an Ir alloy specimen with a series of spherical indenters ranging in size from 14 μm to 1600 μm. Their data are shown in **Figure 5**, where the observed hardness is plotted as a function of the contact radius, a , normalized with respect to the indenter radius, R . For purposes of development, it is useful to think of the horizontal axis as a measure of the depth of penetration of the sphere into the material. The data clearly show that for all of the different spherical indenters, the hardness increases with depth of penetration. This effect, which is observed at both macroscopic and microscopic scales, results from the fact that a spherical indenter is not geometrically self-similar. Rather, the strain induced in the material increases with depth, and so the hardness also increases if the material work hardens (Ir exhibits large work hardening).

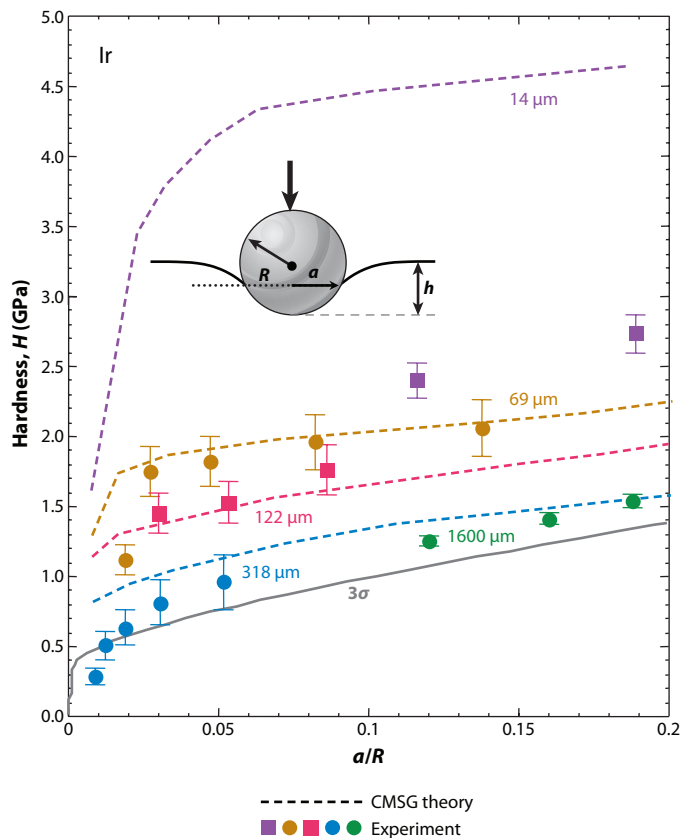


Figure 5

The indentation size effect (ISE) for spherical indenters (41). The data were obtained in an Ir alloy using diamond, steel, and sapphire spheres ranging in radius from 14 μm to 1600 μm . The ISE is manifested not through the depth of penetration but rather through the size of the sphere, with smaller spheres producing greater hardnesses. The dashed lines reflect the predictions of a finite element model that incorporates the strain gradient effects (30, 45). The experimental results and model predictions are in good agreement for the larger spheres, but for the smallest sphere ($R = 14 \mu\text{m}$), the model significantly overestimates the hardness. This finding has been interpreted to indicate a breakdown in the Nix-Gao mechanism for very small spheres (41, 46, 47). CMSG theory, conventional mechanism-based strain gradient plasticity theory.

However, with respect to the ISE, the more interesting behavior concerns the influence of the size of the indenter on the hardness: Specifically, as the radius of the indenter decreases, the hardness increases. Thus, once again smaller is stronger, but in this case, smaller refers to the radius of the sphere rather than to the depth of penetration. The curve at the bottom of the plot labeled 3σ is a prediction of the hardness based on tensile test data by applying Tabor's methods (42). The larger indenter radii give hardnesses that are roughly consistent with the Tabor predictions, but the smaller indenters produce higher hardnesses. As the radius decreases, the curves shift upward, with the effects deviating measurably from macroscopic behavior for indenter sizes of approximately 100 μm and less. Other data demonstrating hardness increases for small spherical indenters have been obtained by Lim & Chaudhri (43) and Durst et al. (44).

As for the case of geometrically self-similar indenters, the ISE for spheres can also be mechanically understood by the Nix-Gao mechanism. Modifying the geometry shown in **Figure 3a**

to account for spherical contact but leaving the rest of the assumptions the same, Swadener et al. (41) showed that the primary results of the Nix-Gao model also apply to a sphere, provided that the characteristic depth, b^* , is replaced by a characteristic radius, R^* , where $R^* = 1/b\rho_s$ or $R^* = \bar{r}/b\rho_s$ if the Nye factor is included. The depth dependency of hardness for spherical indenters is thus a result of classic work-hardening effects, whereas the ISE shifts the curves upward for smaller indenter radii.

Qu et al. (45) present a detailed study of indenter radii effects using a finite element model that incorporates the extra hardening caused by the Nix-Gao mechanism. Their approach is based on the theory of CMSG (conventional mechanism-based strain gradient plasticity) developed by Huang et al. (30) that includes a strain gradient term in the constitutive model based on the Nix-Gao mechanistic framework. The basic material input needed to implement the model is the macroscopic tensile stress-strain curve, which has been measured experimentally for Ir. Predictions of the model assuming a Taylor hardening coefficient $\alpha = 1/3$ are included in **Figure 5**. Comparison with the data shows generally good agreement between theory and experiment, with the exception of the smallest indenter, $R = 14\ \mu\text{m}$, for which the model significantly overestimates the experimental observations. This observation and several others like it have led some researchers to suggest that the Nix-Gao model breaks down when the contact size is very small (41, 46, 47).

CMSG: conventional mechanism-based strain gradient plasticity

CSM: continuous stiffness measurement

Shortcomings of the Nix-Gao Model

Despite its widespread application and general predictive capabilities, the Nix-Gao model does have several important shortcomings. One that has received a great deal of attention is the assumption that the radius of the hemispherical zone in which the GNDs reside is equal to the radius of the contact impression (see **Figure 3**). Swadener et al. (41) argued that this assumption, although attractive because it makes the modeling mathematically tractable, is artificial because it ignores important physical processes that determine the size of the zone. Specifically, if the GNDs were all of similar sign, then constraining them in a small volume would result in large, mutually repulsive forces that would tend to drive them outward to occupy a larger volume. From this perspective, one might expect the relationship between ρ_G and $1/b$ in Equation 3 to break down at some small scale, with the real volume in which the dislocations reside being larger than that assumed in the model. The model would then work in a limited range, but for very shallow pyramidal indentations or indentations made with very small spheres, it would overestimate the hardness because the real GND densities would be smaller. Indeed, this argument has been used to explain why the finite element predictions in **Figure 5** for the small 14- μm spherical indenter are too high (45, 46).

Other experimental observations supporting the notion that the Nix-Gao model breaks down at small scales come from experiments with pyramidal indenters. **Figure 6** shows the depth dependencies of the hardness for MgO and Ir obtained with a Berkovich indenter (41, 47). In **Figure 6**, the data are presented as H^2 versus $1/b$ to examine the adequacy of the Nix-Gao relation. Both plots show a linear-like regime at larger b (smaller $1/b$), but the linear behavior deviates significantly at smaller b (larger $1/b$), with linear extrapolation of the larger-depth data considerably overestimating the small-depth hardnesses. Of course, smaller hardnesses would be expected if the GNDs were to spread to a larger volume. However, the hardness data in **Figure 6** were obtained using a special nanoindentation measurement technique known as continuous stiffness measurement (CSM), which in some materials, especially soft metals, produces significant errors in hardness at small depths in a manner that is consistent with the form of the data in the figure (26, 27). Thus, the observed breakdown in linearity may actually be an experimental artifact.

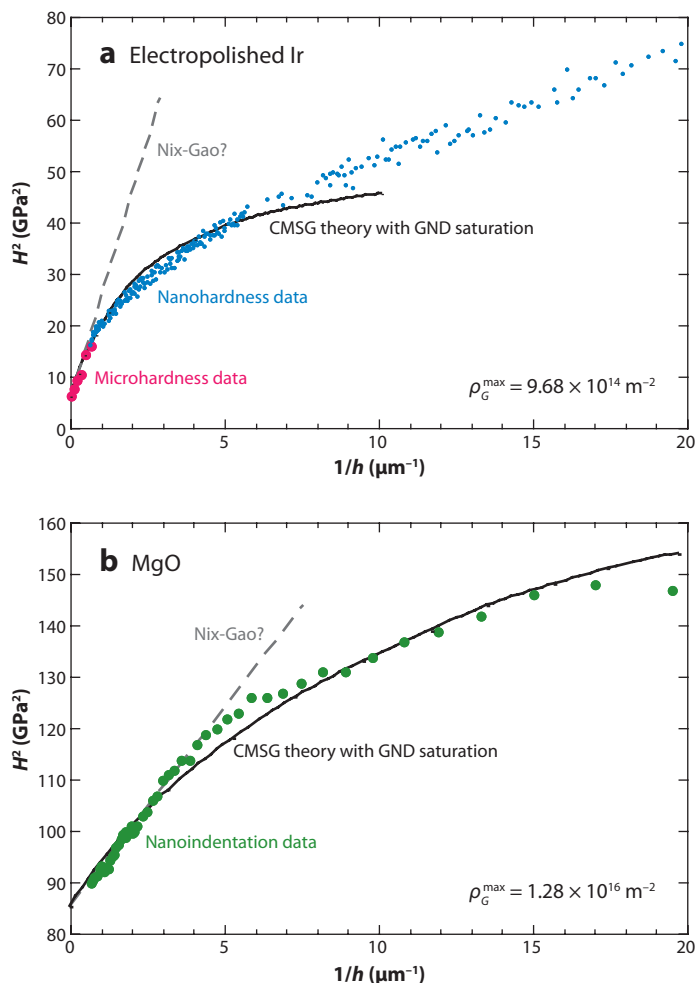


Figure 6

Depth dependency of the hardness for (a) Ir and (b) MgO obtained with a Berkovich pyramidal indenter plotted as H^2 versus $1/h$ to examine the adequacy of the Nix-Gao model (41, 47). The deviation from linearity at small h (large $1/h$) has been interpreted to mean that the Nix-Gao model breaks down at small depths of penetration (41, 46, 47). The solid lines are predictions of CMSG (conventional mechanism-based strain gradient plasticity) theory, assuming that the dislocation density saturates at an upper limit that is determined by curve fitting (46). GND, geometrically necessary dislocation.

The data in **Figure 6** can also be interpreted as being bilinear, that is, a transition between two different linear behaviors. Numerous observations of this sort have been reported (41, 47–53) and are often interpreted as indicating that another mechanism predominates at very small depths—depths of the order of 100 nm. A variety of reasons for the breakdown have been suggested; these include the spreading of the GNDs to a larger volume (41, 47) as well as dislocation source-limited behavior, that is, a change in behavior due to a lack of dislocation sources when the deformation volume is small (48–50). The latter can lead to important changes in the arrangement and density of the GNDs and can thus change the predominant mechanism of hardening (48–50).

From a modeling perspective, one way to account for the expansion of the GND volume is to place an upper limit on the GND density that can be achieved, which is equivalent to letting the GND density saturate. This seems physically reasonable because recovery processes usually cap the dislocation densities that can develop during the normal strain hardening of metals. Huang et al. (46) have incorporated such effects into their CMSG finite element approach by assuming there is an upper limit to the GND density. The limit is derived empirically by seeking the value that best fits experimental data. As shown in **Figure 6**, applying their model to the Ir and MgO data gives reasonable fits to the hardness data, provided that ρ_G saturates at approximately $1 \times 10^{15} \text{ m}^{-2}$ for Ir and at approximately $1 \times 10^{16} \text{ m}^{-2}$ for MgO. Because a dislocation density of $1 \times 10^{15} \text{ m}^{-2}$ is on the high end of what is achievable during the normal strain hardening of metals (54), the saturation argument seems plausible for Ir, but not for MgO. However, recall that for both materials, the bilinear behavior may not be real, but rather an artifact of the nanoindentation testing techniques.

A different approach to determining how large the GND volume really is has been taken by Durst et al. (24), who assumed that the radius of the hemisphere in the Nix-Gao model is not necessarily equal to the contact radius but scales with it by a material-dependent factor, f . The value of f can be determined by fitting experimental data but can also be estimated by conventional finite element modeling of the size of the plastic zone (24). On the basis of experimental studies in several materials (24, 27, 44, 54, 55), Durst et al. (24) found that the value of f usually falls in the range of 1.5 to 2.5 and that good agreement is achieved between the observed ISE and the modified Nix-Gao model predictions; i.e., plots of H^2 versus $1/b$ are very linear. However, until investigators develop a physically based model that explains the assumed proportionality between the contact radius and the GND zone radius, this explanation, like the GND saturation hypothesis, must be viewed largely as empirical.

MICROSTRUCTURAL OBSERVATIONS

One of the keys to establishing the mechanistic origins of the ISE lies in observations of dislocation microstructures and how they vary with indentation size. Unfortunately, such observations are not easy because of the complexity of the techniques required to image dislocations at the requisite (submicrometer) scale. The techniques that have proven most useful are small-scale diffraction methods, including microfocus X-ray diffraction at synchrotron X-ray sources (56–59), backscattered electron diffraction (EBSD) in high-resolution scanning electron microscopes (SEM) (7, 49, 50, 60–62), and convergent beam electron diffraction (CBED) in scanning transmission electron microscopes (STEM) (63). All three techniques can be performed in a scanning mode so as to map the local lattice orientations with submicrometer spatial resolution. The resulting lattice curvature determined from such maps can be used to evaluate the Nye dislocation tensor, which provides a measure of the local GND densities (57, 58, 60, 61). The SEM-based techniques provide information mostly from the surface, whereas the synchrotron-based methods can probe a three-dimensional volume and obtain subsurface information as well. In all cases, focused ion beam (FIB) milling to prepare indentations in cross section has proven to be a key enabling technology. In addition to microdiffraction techniques, microstructural information has also been gleaned by dislocation etch pitting methods (55) and transmission electron microscopy (TEM) studies (7, 48, 50, 63–66), although for TEM, the dislocation densities are often too high to effectively resolve the relevant features in the microstructure.

To date, studies of indentation dislocation microstructures have been quite limited and are not yet extensive enough to draw firm conclusions, but a number of interesting observations are emerging. The most important findings concern the organization of the GND structures beneath the hardness impressions and how they evolve with depth of penetration. Panels a and b of **Figure 7**

EBSD: backscattered electron diffraction

CBED: convergent beam electron diffraction

STEM: scanning transmission electron microscopy (microscope)

FIB: focused ion beam

TEM: transmission electron microscopy (microscope)

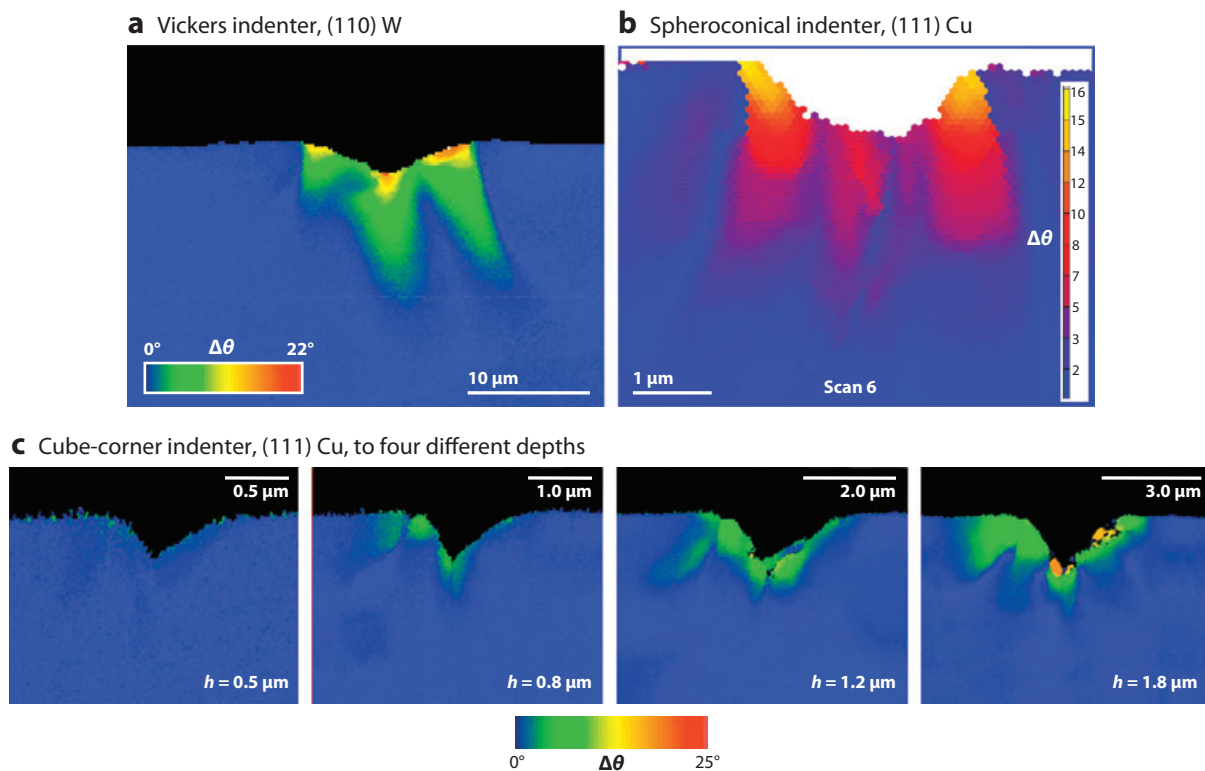


Figure 7

Subsurface lattice rotations beneath small indentations in single crystals used to deduce the local GND (geometrically necessary dislocation) structure. (a) (110) W indented with a Vickers indenter. Used with permission from Reference 62. (b) (111) Cu indented with a conical indenter with a spherical tip ($R = 1 \mu\text{m}$). Used with permission from Reference 56. (c) A series of indentations in (111) Cu made with a cube-corner indenter to depths ranging from $0.5 \mu\text{m}$ to $1.8 \mu\text{m}$ showing the evolution of the GND structure. Used with permission from Reference 67. The very well defined boundaries between regions of different orientations indicate that the GNDs are not homogeneously distributed. The series of micrographs in panel c demonstrates that the GND structure does not develop in a geometrically self-similar fashion.

show cross sections of indentations made in a (110) W single crystal with a Vickers indenter (7, 62) and in a (111) Cu single crystal with a spheroconical indenter having a tip radius of approximately $1 \mu\text{m}$ (60). A spheroconical indenter is a conical indenter with a spherical radius ground on the tip. Both panels a and b of **Figure 7** provide maps of the local crystal misorientations, $\Delta\theta$, based on EBSD measurements. One striking feature in each panel is the distinct patterning of the lattice rotations into regions with very well defined boundaries, indicating that the GNDs are not homogeneously distributed but are organized into small-angle boundaries across which most of the lattice misorientation needed to form the hardness impression is achieved. This indicates that the distribution of the GNDs is not at all like that assumed in the Nix-Gao model, i.e., uniformly distributed in a hemispherical volume, but more like that in a subgrain structure. As a result, the strengthening due to the GNDs may not be well modeled by the Taylor hardening mechanism, and alternative descriptions based on the interaction of glissile dislocations with the small-angle boundaries may be required (50).

Another notable observation from microstructural studies is that, even with geometrically self-similar indenters, the dislocation structure does not develop with indentation depth in a

self-similar way. Rather, as several studies (49, 50, 60, 61, 67) show, the evolution of the GND structure occurs gradually, like that shown in the series of micrographs in **Figure 7c** for indentations made to four different depths in a (111) Cu single crystal with a cube-corner indenter—a sharp triangular pyramid with a centerline-to-face angle of 35.3° (67). Clearly, geometric self-similarity is not obeyed in the development of GND structure, and this behavior probably contributes to the ISE. Observations like these have prompted some researchers to suggest that the evolution of the GND microstructure results from dislocation source limitation. That is, until the contact becomes large enough, the number of dislocation sources that can be activated to accommodate the plastic deformation may be severely limited due to the discrete nature of the sources. In fact, there is some experimental evidence that when dislocation loops are nucleated from a limited number of sources, they may travel long distances into the material without entanglement, giving rise to an entirely different type of GND structure and to a different type of hardening behavior (48, 50, 67). This evidence has been used to explain the bilinear behavior in H^2 -versus- $1/b$ plots as well as the absence of measurable lattice misorientations at small indentation depths (see **Figure 7c**).

Another important observation from studies of subsurface lattice rotations concerns the magnitudes of the overall rotations and their gradients, as well as how they relate to the dependency of the GND density on the size of the indentation. Using EBSD and CBED as imaging tools, several groups have reported that the GND density in Cu deduced from the lattice rotation fields increases as the size of the contact increases, both for spheroconical indenters (61) and for pyramidal indenters (62, 63). This is in direct contrast to the Nix-Gao mechanism, which is predicated on the assumption that the GND density is larger for smaller hardness impressions. In contrast, synchrotron-based microdiffraction X-ray experiments in Cu (59) and etch pitting studies on CaF_2 , in which the etch pit density was determined by atomic force microscopy imaging (55), have shown that the dislocation density increases for smaller indentations. The origin of these discrepancies is not yet apparent and demonstrates a need for more experimental work. One point worth noting is that etch pitting studies reveal not just the GND structure but the entire dislocation structure, thus reminding us that studies focused on the behavior of the SSDs may be equally important in elucidating mechanisms.

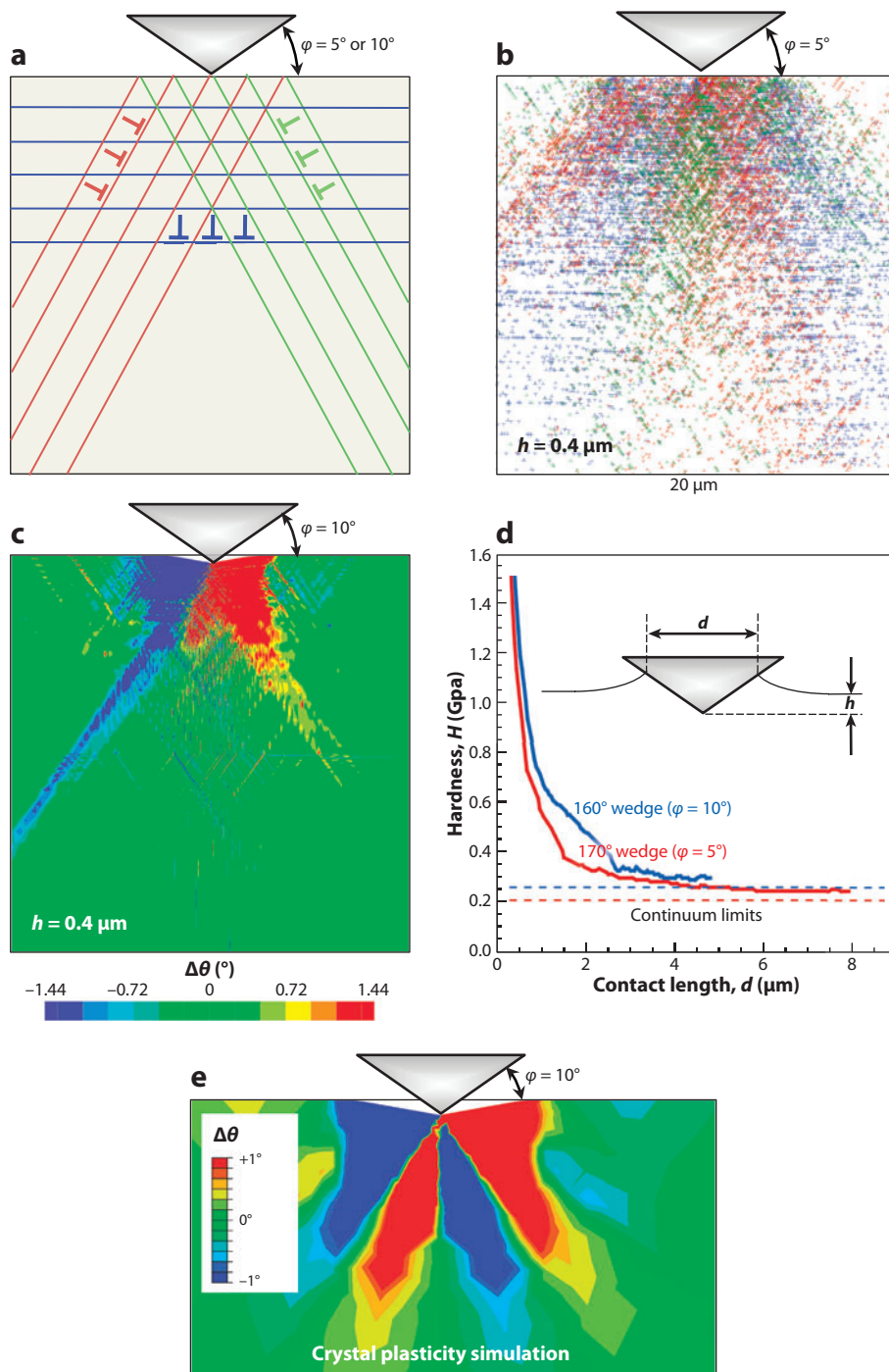
DISLOCATION DYNAMICS SIMULATIONS

Important clues to the origin of the ISE have also been obtained through computer simulation and modeling of dislocation processes based on dislocation dynamics principles (68–74). In such simulations, dislocations can be either randomly placed in the initial microstructure or created by the activation of dislocation sources. A good example is shown in **Figure 8**, which presents the results of a two-dimensional simulation performed by Balint et al. (73) for the activity of edge dislocations during indentation with a rigid wedge. Edge dislocations were allowed to slip on three separate slip planes oriented at $\pm 35.3^\circ$ and 90° with respect to the indentation direction (see **Figure 8a**), multiplying from sources placed randomly in the microstructure. Although the simulations actually modeled the behavior of a film on a rigid substrate, in one case, the film was thick enough to represent bulk behavior.

Results for the thick film are shown in **Figure 8b–d**. **Figure 8b** presents the equilibrium distribution of dislocations in color-coded fashion so as to distinguish activity on each of the three slip planes. The distribution of the three types of dislocations is not random but highly clustered, indicating a preponderance of one type of dislocation in a given region. Indeed, **Figure 8c** shows that the dislocation processes lead to discrete misorientations of the lattice, with abrupt changes in the sign and/or magnitude of the lattice rotation, indicating that the GNDs tend to localize near

Figure 8

Results of two-dimensional dislocation dynamics simulations by Balint et al. (73). (a) The simulation geometry for indentation with a wedge, showing the three independent slip systems. (b) The equilibrium distribution of dislocations for indentation with a 170° wedge ($\phi = 5^\circ$), color-coded according to the three different slip systems. (c) The lattice misorientations produced by a 160° wedge ($\phi = 10^\circ$), indicating discrete regions separated by well-defined boundaries. (d) The hardness versus depth, which exhibits a strong indentation size effect. Panels a–d used with permission from Reference 73. For comparison, panel e shows the lattice rotations for a 160° wedge ($\phi = 10^\circ$) predicted by crystal plasticity finite element simulation.



boundaries. However, the simulation does not inherently distinguish between GNDs and SSDs; in the end, the GNDs can be identified only through the local lattice misorientations they produce. The corresponding depth dependency of the hardness, shown in **Figure 8d**, exhibits a distinct ISE of the type observed in experiment, decreasing from a large value at small depths toward a lower asymptotic value at large depths that represents the hardness observed in the continuum crystal plasticity limit. Close inspection of the simulation results reveals that the ISE is largely source limited; that is, in the initial stages of indentation, large stresses are needed to activate the dislocation sources, but once some dislocation activity commences and enough dislocation multiplication takes place, the flow stress decreases toward a steady-state value determined by an equilibrium of nucleation, multiplication, and annihilation processes.

For comparison, we have included in **Figure 8e** the in-plane lattice rotation field for indentation with a 160° wedge computed from continuum crystal plasticity finite element simulations, adopting the same slip systems and slip strength of 50 MPa used by Balint et al. (73). Comparison to **Figure 8c** shows that the subsurface rotation sectors are distinctly different from the dislocation dynamics simulations—the latter show only one boundary that separates positive and negative rotations. The continuum crystal plasticity predictions are, however, qualitatively similar to the wedge indentation experiments by Kysar et al. (75). This suggests that the dislocation dynamics simulations predict a GND structure that is predominantly governed by the dislocation source densities, whereas in continuum simulations and microindentation experiments, the GND structures are determined by the orientations of slip systems.

The value of dislocation dynamics simulations is that details of the controlling mechanisms can be obtained by carefully analyzing and examining the results. However, two-dimensional simulations inherently ignore some important three-dimensional effects, specifically, the bowing and entanglement of dislocations that can lead to significant hardening and irreversibility of plastic deformation. Thus, two-dimensional dislocation dynamics simulations should be viewed as illuminative of mechanisms rather than as quantitatively predictive.

Figure 9 illustrates another good example of the value of discrete dislocation modeling. Here, the results of a simple two-dimensional simulation conducted by Kreuzer & Pippan (71) are shown. In the simulation, positive and negative edge dislocations in an originally random distribution were allowed to glide only on the horizontal plane in response to the stresses induced by a 140° wedge indenter. Although overly simplistic, the simulation illustrates an important point about the development of discrete lattice misorientations and the role of GNDs in creating them. Specifically, the equilibrium distribution of dislocations in **Figure 9a** shows that there are three dense vertical bands: one at the vertex of the indenter and the other two near the contact edges. The dislocations in the center band are predominantly negative edge in character, whereas those at the contact edges are positive. Thus, as shown in **Figure 9b**, the applied stresses generated by the indenter naturally rearrange the dislocations into discrete tilt boundaries, with the alternating positive and negative boundaries accommodating the lattice rotation imposed by the indenter, as illustrated by the bending of the horizontal planes. This means that an initially random array of positive and negative edge dislocations can naturally dissociate into well-defined tilt boundaries composed of the GNDs needed to accommodate the volume displaced by the indenter. However, the process does not require that the GNDs be generated; rather, they are formed by the separation of existing dislocations into groups, with the stresses of the indenter and the natural interdislocation forces driving the separation. Therefore, it does not necessarily follow that all the GNDs must be nucleated or generated during the indentation process. Moreover, along with the crystal plasticity finite element results presented above, there appears to be a natural explanation for the inhomogeneous GND structures that form and develop during the indentation of single-crystalline metals with geometrically self-similar indenters.

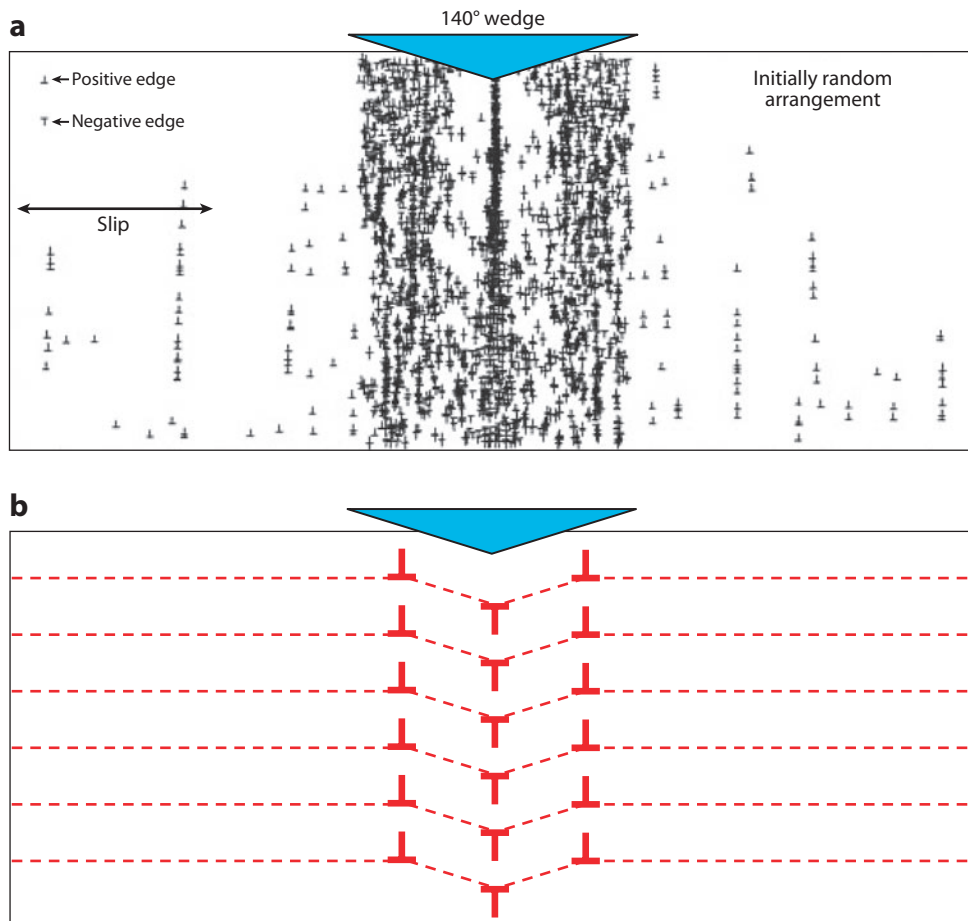


Figure 9

Results of two-dimensional discrete dislocation dynamics simulations conducted by Kreuzer & Pippan (71). The starting configuration consists of a random array of equal numbers of positive and negative edge dislocations gliding on the horizontal plane with no dislocation sources. (a) The simulation geometry for indentation with a 140° wedge and the equilibrium distribution of dislocations under load. (b) A schematic representation of the structure of the tilt boundaries and how they accommodate the lattice rotations imposed by the indenter. Adapted with permission from Reference 71.

Lastly, we note that the simulations in **Figure 9** exhibit essentially no ISE. However, when discrete dislocation sources are added to the starting configuration, a strong ISE is observed (68). This finding once again indicates that dislocation source limitation is a potentially important mechanism for the ISE.

IMPORTANT EXPERIMENTAL CONSIDERATIONS

Before closing, we wish to provide some insight based on our testing experience about the problems that can be encountered in obtaining meaningful measurements of hardness at small depths by nanoindentation. Such measurements are not necessarily straightforward; there are

numerous potential mistakes that can produce experimental artifacts and affect the interpretation of data for the ISE.

Specimen Preparation

As discussed above, specimen preparation is of paramount importance in obtaining quality experimental data for the ISE. There are three key specimen preparation issues: (a) surface contamination, e.g., oxides, thin organic layers, and contaminants; (b) mechanical damage from surface preparation; and (c) surface roughness.

First, surface contaminants affect the quality of data in obvious ways. If there is a thin surface film with a hardness different from that of the bulk specimen, e.g., a thin, hard surface oxide, then there will be a measured change in hardness with depth, but not one that is intrinsic to the material. Films of only a few tens of nanometers are quite common in practice and can significantly affect hardnesses measured in the range of 50 nm to 500 nm. Because of this, it is imperative that experiments be performed in materials that are not prone to contamination or oxidation. Cleaning is also important because residual organic residue that is not carefully removed prior to testing can affect the data.

Second, as illustrated by the Cu data in **Figure 2**, mechanical damage from surface preparation is an extremely important factor that is often overlooked in hardness measurement. Preparing surfaces that are free from mechanical damage requires more than just a good surface finish; care must also be taken to assure that, during successive grinding and polishing steps, the damage from previous steps is adequately removed (28). If not, there can be an increase in hardness at small depths due to the work-hardened layers at the surface. Electropolishing can be used to obviate many of these problems, provided that it does not alter the chemistry of the surface and that care is taken to assure that adequate material is removed (12, 23).

Finally, surface roughness is also an often-overlooked issue, but one that is crucial to obtaining meaningful measurements. In the measurement of hardness by any method at any scale, accurate and meaningful measurements can be made only in the limit that the indentation depth is large in comparison to the surface roughness (23, 25, 53, 76, 77). Nanoindentation methods present an additional complication in that procedures for computing the contact area used to determine the hardness are premised on the assumption that the surface is perfectly flat (17). When the surface is flat, the known shape of the indenter, as described by its area function in conjunction with the measured depth of penetration and the contact stiffness, can be used to determine the contact area and thus the hardness. However, when the surface is rough at the scale of the contact dimension, the contact area determined in this way can be in significant error. Such effects usually produce increased scatter in the data, so it is imperative that enough measurements be made to assure a statistically significant mean. In addition, if the surface is too rough, the roughness may contribute to the ISE because smoothing the roughness during the initial stages of deformation changes the contact geometry (77).

Indenter Area-Function Calibration

As mentioned in the previous section, accurate determination of hardness by nanoindentation methods requires a precise knowledge of the shape of the indenter as described by its area function (17). The area function, which relates the cross-sectional area of the indenter to the distance from the tip, is rarely that for a perfect pyramid, and the influences of tip rounding and blunting can be very important in making accurate hardness measurements at small depths. The area function is

most commonly determined by conducting experiments in a calibration material like fused silica (amorphous), in which the hardness is essentially independent of depth and the elastic properties are well known (17). It is imperative that the area function be well calibrated because errors in the area function translate directly into errors in contact area and hardness. As an example, when a Berkovich indenter that has some tip rounding is used to make hardness measurements in a material in which there is no ISE, but it is assumed that the area function is that for a perfect pyramid, the nanoindentation hardness will overestimate the true hardness in a manner that increases with decreasing depth. Thus, an ISE will be observed in a material in which there really is none.

One simple way to check on whether the area function is correct is to use the nanoindentation procedures to measure the elastic modulus as well. Because modulus is a structure-insensitive property, any observed change in modulus with depth must raise suspicions that the area function is in error. Errors in the measured compliance of the testing system can lead to similar problems, but with most commercial nanoindentation testing systems, these usually occur only at loads and depths larger than those of interest in studies of the ISE (78).

Indenter tip blunting can also lead to an apparent ISE in a totally different way. If the tip is too blunt, then contact at small depths may be more spherical in nature than pyramidal. This is important because indentation with a sphere transitions from elastic contact at small depths to fully developed plastic contact at large depths (42), and the transition is accompanied by a change in contact mechanics that produces a geometrically induced ISE rather than one resulting from material behavior (79, 80). Thus, one must ensure that the tip is not so blunt that these effects become important. As documented elsewhere, the exact conditions needed to achieve fully developed plasticity during spherical contact are a function of the elastic and plastic properties of the material and the indenter radius (42, 79–81).

Special Issues in Nanoindentation Testing

In addition to the problems discussed above, there are also a few special issues in nanoindentation testing that are often overlooked and can lead to important inaccuracies in hardness measurement at small depths. One is accurate determination of the zero point, or the point at which the indenter first makes contact with the surface. Various schemes have been developed to do this; most of them are based on changes in the measured stiffness when the indenter makes contact with the specimen (15, 17). However, because some finite depth of penetration is needed to achieve this condition, there is always some uncertainty in the exact location of the zero point. As a result, the relative error in the depth measurement increases systematically as the contact size decreases, producing an apparent ISE. Clearly, then, accurate hardness measurements at small depths require that special attention be given to precisely locating the surface. At the very least, investigators should estimate how large this error may be and should incorporate it into the error bars in their hardness measurements.

A final issue concerns the use of CSM techniques to measure hardness at small depths. These techniques use small oscillations in the load or displacement to make continuous measurements of the contact stiffness as the indenter is driven into the material (17). The advantage is that the hardness can be measured continuously as a function of depth in a single experiment. However, it has recently been shown that this technique can be subject to large errors when applied at small depths in many materials, including most soft metals (26). In fact, it has been argued that the apparent bilinear behavior observed in **Figure 6** is not real but an artifact of CSM measurement problems (26, 27). In light of these observations, we do not recommend the use of CSM techniques in their current state of development for characterization of the ISE.

DISCLOSURE STATEMENT

The authors have received research funding in the past three years from Agilent Technologies, a manufacturer of nanoindentation testing equipment. One of the authors (E.G.H.) was previously employed by Agilent Technologies.

ACKNOWLEDGMENTS

This work was sponsored by the National Science Foundation under contract CMMI-0800168 (G.M.P. and Y.G.) and by the Division of Materials Sciences and Engineering, U.S. Department of Energy (G.M.P. and Y.G.). G.M.P. wishes to gratefully acknowledge the Alexander von Humboldt Foundation for fellowship support during the period in which the manuscript was prepared.

LITERATURE CITED

1. Mott BW. 1957. *Microindentation Hardness Testing*. London: Butterworths
2. Bückle H. 1959. Progress in microindentation hardness testing. *Metall. Rev.* 4:49–100
3. Gane N. 1970. The direct measurement of the strength of metals on a submicrometer scale. *Proc. R. Soc. Lond. Ser. A* 317:367–91
4. Upit GP, Varchenya SA. 1973. The size effect in the hardness of single crystals. In *The Science of Hardness Testing and Its Research Applications*, ed. JH Westbrook, H Conrad, 10:135–46. Metals Park, OH: ASM
5. Chen CC, Hendrickson AA. 1973. Microhardness phenomena in silver. In *The Science of Hardness Testing and Its Research Applications*, ed. JH Westbrook, H Conrad, 21:274–90. Metals Park, OH: ASM
6. Tabor D. 1986. Indentation hardness and its measurement: some cautionary comments. In *Microindentation Techniques in Materials Science and Engineering. ASTM STP 889*, ed. PJ Blau, BR Lawn, pp. 129–59. Philadelphia: ASTM
7. Kiener D, Durst K, Rester M, Minor AM. 2009. Revealing deformation mechanisms with nanoindentation. *J. Met.* 61:14–23
8. Gerberich WW, Tymiak NI, Grunlan JC, Horstemeyer MF, Baskes MI. 2002. Interpretations of indentation size effect. *J. Appl. Mech.* 69:433–42
9. Bull SJ. 2003. On the origins of the indentation size effect. *Z. Metallkd.* 94:787–92
10. Zhu TT, Bushby AJ, Dunstan. 2008. Materials mechanical size effects: a review. *Mater. Tech.* 23:193–209
11. Sangwal K. 2000. On the reverse indentation size effect and microhardness of solids. *Mater. Chem. Phys.* 63:145–52
12. Bull SJ, Page TF, Yoffe EH. 1989. An explanation of the indentation size effect in ceramics. *Philos. Mag. Lett.* 59:281–88
13. Li H, Bradt RC. 1993. The microhardness indentation load/size effect in rutile and cassiterite single crystals. *J. Mater. Sci.* 28:917–26
14. Bushby AJ, Dunstan DJ. 2004. Plasticity size effects in nanoindentation. *J. Mater. Res.* 19:137–42
15. Pethica JB, Hutchings R, Oliver WC. 1983. Hardness measurements at penetration depths as small as 20 nm. *Philos. Mag.* A48:593–606
16. Pharr GM, Oliver WC. 1989. Nanoindentation of silver: relations between hardness and dislocation structure. *J. Mater. Res.* 4:94–101
17. Oliver WC, Pharr GM. 1992. An improved technique for determining hardness and elastic modulus by load and displacement sensing indentation experiments. *J. Mater. Res.* 7:1564–83
18. Stelmashenko NA, Walls MG, Brown LM, Milman YV. 1993. Microindentations on W and Mo oriented single crystals: an STM study. *Acta Metall. Mater.* 41:2855–65
19. Tangyunyong P, Thomas RC, Houston JE, Michalske TA, Crooks RM, Howard AJ. 1993. Nanometer-scale mechanics of gold films. *Phys. Rev. Lett.* 71:3319–22
20. Ma Q, Clarke DR. 1995. Size dependent hardness of silver single crystals. *J. Mater. Res.* 10:853–63
21. Poole WJ, Ashby MF, Fleck NA. 1996. Microhardness of annealed and work-hardened copper polycrystals. *Scr. Mater.* 34:559–64

22. McElhaney KW, Vlassak JJ, Nix WD. 1998. Determination of indenter tip geometry and indentation contact area for depth-sensing indentation experiments. *J. Mater. Res.* 13:1300-6
23. Liu Y, Ngan AHW. 2001. Depth dependence of hardness in copper single crystals measured by nanoindentation. *Scr. Mater.* 44:237-41
24. Durst K, Backes B, Göken M. 2005. Indentation size effect in metallic materials: correcting for the size of the plastic zone. *Scr. Mater.* 52:1093-97
25. Pathak S, Stojakovic D, Doherty R, Kalidindi SR. 2009. Importance of surface preparation on the nano-indentation stress-strain curves measured in metals. *J. Mater. Res.* 24:1142-55
26. Pharr GM, Strader JH, Oliver WC. 2009. Critical issues in making small-depth mechanical property measurements by nanoindentation with continuous stiffness measurement. *J. Mater. Res.* 24:653-66
27. Durst K, Franke O, Böhner A, Göken M. 2007. Indentation size effect in Ni-Fe solid solutions. *Acta Mater.* 55:6825-33
28. Petzow G. 1999. *Metallographic Etching: Techniques for Metallography, Ceramography, and Plastography*. New York: ASM. 2nd ed.
29. Nix WD, Gao H. 1998. Indentation size effects in crystalline materials: a law for strain gradient plasticity. *J. Mech. Phys. Solids* 46:411-25
30. Huang Y, Qu S, Hwang KC, Li M, Gao H. 2004. A conventional theory of mechanism-based strain gradient plasticity. *Int. J. Plast.* 20:753-82
31. Gao H, Huang Y, Nix WD, Hutchinson JW. 1999. Mechanism-based strain gradient plasticity. I. Theory. *J. Mech. Phys. Solids* 47:1239-63
32. Huang Y, Gao H, Nix WD, Hutchinson JW. 1999. Mechanism-based strain gradient plasticity. II. Analysis. *J. Mech. Phys. Solids* 48:99-128
33. Bassani JL. 2001. Incompatibility and a simple gradient theory of plasticity. *J. Mech. Phys. Solids* 49:1983-96
34. Evers LP, Parks DM, Brekelmans WAM, Geers MGD. 2002. Crystal plasticity model with enhanced hardening by geometrically necessary dislocation accumulation. *J. Mech. Phys. Solids* 50:2403-24
35. Fleck NA, Muller GM, Ashby MF, Hutchinson JW. 1994. Strain gradient plasticity: theory and experiment. *Acta Metall. Mater.* 42:475-87
36. Fleck NA, Hutchinson JW. 2001. A reformulation of strain gradient plasticity. *J. Mech. Phys. Solids* 49:2245-71
37. Gudmundson P. 2004. A unified treatment of strain gradient plasticity. *J. Mech. Phys. Solids* 52:1379-406
38. Fleck NA, Hutchinson JW. 1993. A phenomenological theory for strain gradient effects in plasticity. *J. Mech. Phys. Solids* 41:1825-57
39. Gurtin ME. 2002. A gradient theory of single-crystal viscoplasticity that accounts for geometrically necessary dislocations. *J. Mech. Phys. Solids* 50:5-32
40. Arsenlis A, Parks DM. 1999. Crystallographic aspects of geometrically-necessary and statistically-stored dislocation density. *Acta Mater.* 47:1597-611
41. Swadener JG, George EP, Pharr GM. 2002. The correlation of the indentation size effect measured with indenters of various shapes. *J. Mech. Phys. Solids* 50:681-94
42. Tabor D. 1951. *The Hardness of Metals*. Oxford, UK: Clarendon Press
43. Lim YY, Chaudhri MM. 1999. The effect of indenter load on the nanohardness of ductile metals: an experimental study on polycrystalline work-hardened and annealed oxygen-free copper. *Philos. Mag.* A79:2979-3000
44. Durst K, Göken M, Pharr GM. 2006. Indentation size effect in spherical and pyramidal indentations. *J. Phys. D* 41:074005
45. Qu S, Huang Y, Pharr GM, Hwang KC. 2006. The indentation size effect in the spherical indentation of iridium: a study via the conventional theory of mechanism-based strain gradient plasticity. *Int. J. Plast.* 22:1265-86
46. Huang Y, Zhang F, Hwang KC, Nix WD, Pharr GM, Feng G. 2006. A model for size effects in nanoindentation. *J. Mech. Phys. Solids* 54:1668-86
47. Feng G, Nix WD. 2004. Indentation size effect in MgO. *Scr. Mater.* 51:599-603
48. Rester M, Motz C, Pippan R. 2009. Where are the geometrically necessary dislocations accommodating small imprints? *J. Mater. Res.* 24:647-51

49. Rester M, Motz C, Pippin R. 2008. Indentation across size scales: a survey of indentation-induced plastic zones in copper {111} single crystals. *Scr. Mater.* 59:742-45
50. Rester M, Motz C, Pippin R. 2007. Microstructural investigation of the volume beneath nanoindentations in copper. *Acta Mater.* 55:6427-35
51. Elmustafa AA, Stone DS. 2002. Indentation size effect in polycrystalline FCC metals. *Acta Mater.* 50:3641-50
52. Elmustafa AA, Stone DS. 2003. Nanoindentation and the indentation size effect: kinetics of deformation and strain gradient plasticity. *J. Mech. Phys. Solids* 51:357-81
53. Zong Z, Luo J, Adewoye OO, Elmustafa AA, Hammad F, Soboyejo WO. 2007. Indentation size effects in the nano and microhardness of FCC single crystal metals. *Mater. Manuf. Proc.* 22:228-37
54. Durst K, Backes B, Franke O, Göken M. 2006. Indentation size effect in metallic materials: modeling strength from pop-in to macroscopic hardness using geometrically necessary dislocations. *Acta Mater.* 54:2457-555
55. Sadrabadi P, Durst K, Göken M. 2009. Study on the indentation size effect in CaF_2 : dislocation structure and hardness. *Acta Mater.* 57:1281-89
56. Yang W, Larson BC, Pharr GM, Ice GE, Budai JD, et al. 2004. Deformation microstructure under microindents in single-crystal Cu using three-dimensional X-ray structural microscopy. *J. Mater. Res.* 19:66-72
57. Larson BC, Tischler JZ, El-Azab A, Liu W. 2008. Dislocation density tensor characterization of deformation using 3D X-ray microscopy. *J. Eng. Mater. Tech.* 130:021024
58. Larson BC, El-Azab A, Yang W, Tischler JZ, Liu W, Ice GE. 2007. Experimental characterization of the mesoscale dislocation density tensor. *Philos. Mag.* 87:1327-47
59. Feng G, Budiman AS, Nix WD, Tamura N, Patel JR. 2008. Indentation size effects in single crystal copper as revealed by synchrotron X-ray microdiffraction. *J. Appl. Phys.* 104:043501
60. Zaaferani N, Raabe D, Singh RN, Roters F, Zaefferer S. 2006. Three-dimensional investigation of the texture and microstructure below a nanoindent in a Cu single crystal using 3D EBSD and crystal plasticity finite element simulations. *Acta Mater.* 54:1863-76
61. Demir E, Raabe D, Zaaferani N, Zaefferer S. 2009. Investigation of the indentation size effect through the measurement of the geometrically necessary dislocations beneath small indents of different depths using EBSD tomography. *Acta Mater.* 57:559-69
62. Kiener D, Pippin R, Motz C, Kreuzer. 2006. Microstructural evolution of the deformed volume beneath microindents in tungsten and copper. *Acta Mater.* 54:2801-11
63. McLaughlin KK, Clegg WJ. 2008. Deformation underneath low-load indentations in copper. *J. Phys. D* 41:074007
64. Zielinski W, Huang H, Venkataraman S, Gerberich WW. 1995. Dislocation distribution under a microindentation into an iron-silicon single crystal. *Philos. Mag.* A72:1221-37
65. Chiu YL, Ngan AHW. 2002. A TEM investigation on indentation plastic zones in $\text{Ni}_3\text{Al}(\text{Cr},\text{B})$ single crystals. *Acta Mater.* 50:2677-91
66. Kramer DE, Savage MF, Lin A, Foecke T. 2004. Novel method for TEM characterization of deformation under nanoindents in nanolayered materials. *Scr. Mater.* 50:745-49
67. Rester M, Motz C, Pippin R. 2008. Stacking fault energy and indentation size effect: Do they interact? *Scr. Mater.* 58:187-90
68. Kreuzer HGM, Pippin R. 2004. Discrete dislocation simulation of nanoindentation: the effect of moving conditions and indenter shape. *Mater. Sci. Eng. A* 387-89:254-56
69. Kreuzer HGM, Pippin R. 2004. Discrete dislocation simulation of nanoindentation. *Comput. Mech.* 33:292-98
70. Kreuzer HGM, Pippin R. 2004. Discrete dislocation simulation of nanoindentation: indentation size effect and the influence of slip band orientation. *Acta Mater.* 55:3229-35
71. Kreuzer HGM, Pippin R. 2005. Discrete dislocation simulation of nanoindentation: the effect of statistically distributed dislocations. *Mater. Sci. Eng. A* 400:460-62
72. Widjaja A, Van Der Giessen E, Needleman A. 2005. Discrete dislocation modeling of submicron indentation. *Mater. Sci. Eng. A* 400:456-59

73. Balint DS, Deshpande V, Needleman A, Van Der Giessen E. 2006. Discrete dislocation plasticity analysis of the wedge indentation of films. *J. Mech. Phys. Solids* 54:2281–303
74. Widjaja A, Van Der Giessen E, Deshpande V, Needleman A. 2007. Contact area and size effects in discrete dislocation modeling of wedge indentation. *J. Mater. Res.* 22:655–66
75. Kysar JW, Gan YX, Morse TL, Chen X, Jones ME. 2007. High strain gradient plasticity associated with wedge indentation into face-centered cubic single crystals: geometrically necessary dislocation densities. *J. Mech. Phys. Solids* 55:1554–73
76. Rodriguez R, Gutierrez I. 2003. Correlation between nanoindentation and tensile properties: influence of the indentation size effect. *Mater. Sci. Eng. A* 361:377–84
77. Kim JY, Kang SK, Lee JJ, Jang JI, Lee YH, et al. 2007. Influence of surface-roughness on indentation size effect. *Acta Mater.* 55:3555–62
78. Oliver WC, Pharr GM. 2004. Measurement of hardness and elastic modulus by instrumented indentation: advances in understanding and refinements to methodology. *J. Mater. Res.* 19:3–20
79. Taljat B, Pharr GM. 2004. Development of pile-up during spherical indentation of elastic-plastic solids. *Int. J. Solids Struct.* 41:3891–904
80. Park YJ, Pharr GM. 2004. Nanoindentation with spherical indenters: finite element studies of deformation in the elastic-plastic transition regime. *Thin Solid Films* 447:246–50
81. Herbert EG, Oliver WC, Pharr GM. 2006. On the measurement of yield strength by spherical indentation. *Philos. Mag.* 86:5521–39



Contents

New Developments in Composite Materials

Biological Composites

John W.C. Dunlop and Peter Fratzl 1

On the Mechanistic Origins of Toughness in Bone

Maximilien E. Launey, Markus J. Buehler, and Robert O. Ritchie25

Teeth: Among Nature's Most Durable Biocomposites

Brian R. Lawn, James J.-W. Lee, and Herzl Chai55

Mechanical Principles of Biological Nanocomposites

Baobua Ji and Huajian Gao77

Optimal Design of Heterogeneous Materials

S. Torquato 101

Physical Properties of Composites Near Percolation

C.-W. Nan, Y. Shen, and Jing Ma 131

Magnetoelectric Composites

G. Srinivasan 153

Self-Healing Polymers and Composites

*B.J. Blaiszik, S.L.B. Kramer, S.C. Olugebefola, J.S. Moore, N.R. Sottos,
and S.R. White* 179

Steel-Based Composites: Driving Forces and Classifications

David Embury and Olivier Bouaziz 213

Metal Matrix Composites

Andreas Mortensen and Javier Llorca 243

Current Interest

The Indentation Size Effect: A Critical Examination of Experimental Observations and Mechanistic Interpretations

George M. Pharr, Erik G. Herbert, and Yanfei Gao 271

Plasticity in Confined Dimensions <i>Oliver Kraft, Patric A. Gruber, Reiner Mönig, and Daniel Weygand</i>	293
Saturation of Fragmentation During Severe Plastic Deformation <i>R. Pippan, S. Scheriau, A. Taylor, M. Hafok, A. Hobenwarter, and A. Bachmaier</i>	319
Ultrasonic Fabrication of Metallic Nanomaterials and Nanoalloys <i>Dmitry G. Shchukin, Darya Radziuk, and Helmuth Möbwald</i>	345
Oxide Thermoelectric Materials: A Nanostructuring Approach <i>Kunibito Koumoto, Yifeng Wang, Ruizhi Zhang, Atsuko Kosuga, and Ryoji Funabashi</i>	363
Inkjet Printing of Functional and Structural Materials: Fluid Property Requirements, Feature Stability, and Resolution <i>Brian Derby</i>	395
Microfluidic Synthesis of Polymer and Inorganic Particulate Materials <i>Jai Il Park, Amir Saffari, Sandeep Kumar, Axel Günther, and Eugenia Kumacheva</i>	415
Current-Activated, Pressure-Assisted Densification of Materials <i>J.E. Garay</i>	445
Heterogeneous Integration of Compound Semiconductors <i>Oussama Moutanabbir and Ulrich Gösele</i>	469
Electrochemically Driven Phase Transitions in Insertion Electrodes for Lithium-Ion Batteries: Examples in Lithium Metal Phosphate Olivines <i>Ming Tang, W. Craig Carter, and Yet-Ming Chiang</i>	501
Electromigration and Thermomigration in Pb-Free Flip-Chip Solder Joints <i>Chih Chen, H.M. Tong, and K.N. Tu</i>	531
The Structure of Grain Boundaries in Strontium Titanate: Theory, Simulation, and Electron Microscopy <i>Sebastian von Alftan, Nicole A. Benedek, Lin Chen, Alvin Chua, David Cockayne, Karleen J. Dudeck, Christian Elsässer, Michael W. Finnis, Christoph T. Koch, Behnaz Rahmati, Manfred Rühle, Shao-Ju Shib, and Adrian P. Sutton</i>	557

Index

Cumulative Index of Contributing Authors, Volumes 36–40	601
---	-----

Errata

An online log of corrections to *Annual Review of Materials Research* articles may be found at <http://matsci.annualreviews.org/errata.shtml>